Terrestrial Radar Interferometric Measurement of Hillslope Deformation and Atmospheric Disturbances in the Illgraben Debris-Flow Catchment, Switzerland

Rafael Caduff, Andrew Kos, Fritz Schlunegger, Brian W. McArdell, and Andreas Wiesmann, *Senior Member, IEEE*

***Abstract*—We describe a method for rapid identification and precise quantification of slope deformation using a portable radar interferometer. A rockslide with creep-like behavior was identified in the rugged and inaccessible headwaters of the Illgraben debris-flow catchment, located in the Central Swiss Alps. The estimated volume of the moving rock mass was approximately 0.5×10^6 m^3 with a maximum daily (3-D) displacement rate of 3 mm. Fast scene acquisition in the order of 6 s/scene led to uniquely precise mapping of spatial and temporal variability of atmospheric phase delay. Observations led to a simple qualitative model for prediction of atmospheric disturbances using a simple model for solar radiation, which can be used for advanced campaign planning for short observation periods (hours to days).**

***Index Terms*—Atmospheric phase delay, rockslide monitoring, terrestrial radar interferometry.**

I. Introduction

FAILURE of bedrock instabilities in steep Alpine catchments result in the transfer of significant quantities of sediment from hillslopes into channels, which can subsequently be entrained by fluvial processes or remobilized as hazardous debris-flows [1], [2]. Remote sensing techniques including aerial photogrammetry and lidar have been used to analyze sediment transfer mechanisms by quantifying the change in ground surface elevation before and after a mass movement event has taken place [3], [4]. Although these techniques yield robust information about transferred volumes and surface changes over mid-term timescales spanning months to years, catchment wide measurements of mm-scale surface deformations on a hourly to daily basis are not possible with these tools. Here, we present a case where a terrestrial radar survey of the steep, rugged Illgraben debris flow catchment (Central Alps of Switzerland) showed the behavior of a creeping rockmass, for which we resolve a displacement field on an hourly basis and precision down to 0.2 mm during periods with low atmospheric phase variability. Measurements are accomplished with a portable radar interferometer, which allows a precise detection of surface-displacements as well as of atmospheric phase-delay variations over short observation time scales down to individual minutes. To avoid highly variable atmospheric phase at the time of the acquisition, a novel proxy is presented allowing the qualitative forecast of atmospheric phase variability

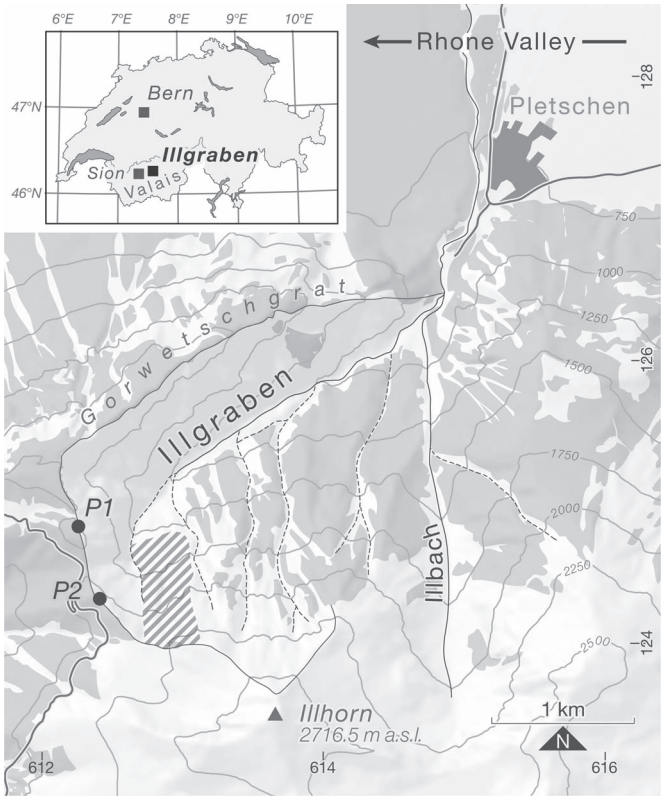

Fig. 1. Location of the Illgraben debris flow catchment showing area of investigation (hatched), position of GPRI for various campaigns (labeled P1 and P2), and forested areas (shaded gray).

Manuscript received June 7, 2012; revised December 1, 2012 and February 18, 2013; accepted April 10, 2013.

This paper has supplementary downloadable material available at http://ieeexplore.ieee.org, provided by the authors. This includes two multimedia AVI format movie clips, which show the spatio-temporal evolution of the interferometric phase differences of the Illgraben site and the spatio-temporal variability on the measured phase differences in comparison to the modeled insolation on the target area. This material is 13.8 MB in size.

R. Caduff and F. Schlunegger are with the Institute for Geology, University of Bern, CH-3012 Bern, Switzerland (e-mail: rafael.caduff@geo.unibe.ch; fritz.schlunegger@geo.unibe.ch).

A. Kos is with the Institute for Geotechnical Engineering, ETH Zürich, CH-8093 Zürich, Switzerland (e-mail: andrew.kos@igt.baug.ethz.ch).

B. W. McArdell is with the Swiss Federal Institute for Forest, Snow and Landscape Research, CH-8903 Birmensdorf, Switzerland (e-mail: brian.mcardell@wsl.ch).

A. Wiesmann is with the Gamma Remote Sensing AG, CH-3073 Gümligen, Switzerland (e-mail: wiesmann@gamma-rs.ch).

Color versions of one or more of the figures in this paper are available online at http://ieeexplore.ieee.org.

Digital Object Identifier 10.1109/LGRS.2013.2264564

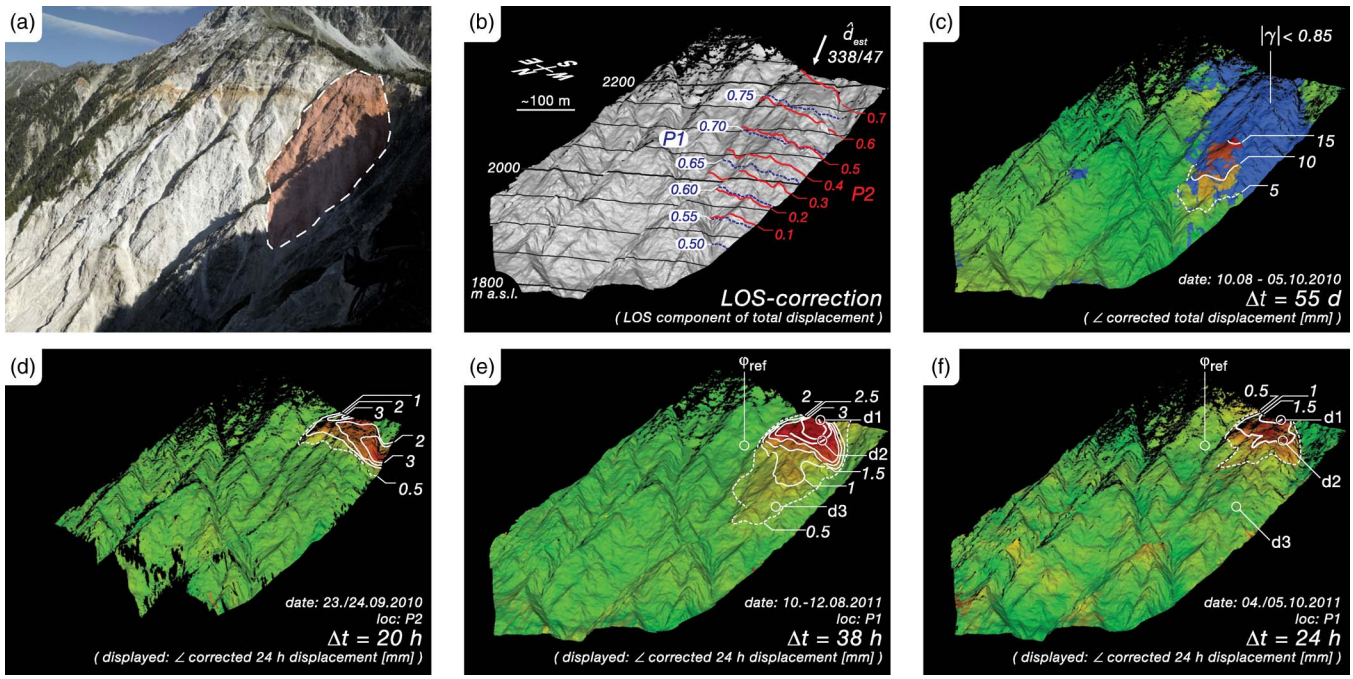

Fig. 2. (a) Photograph taken from P1 of the target rock slope beneath the active escarpment. The outlined area marks the maximal extent of the measured slope instability. (b) Shaded surface model (terrestrial lidar) in same geometry as photograph in (a). Contour Lines P1 and P2 define the LOS fraction of the total displacement. The principal movement direction $\hat{d}_{est}$ estimated from field observations. (c) Total displacements for the period 12.08.2011—05.10.2011. Blue indicates decorrelated areas (coherence coefficient ($|\gamma|$) < 0.85). (d) Corrected daily displacement rates measured from P2. (e) and (f) Corrected daily displacement rates measured from P1.

using a solar radiation model and thus reducing the efforts in postprocessing. We then introduce a geometric correction in a final step, allowing a conversion from line-of-sight (LOS) displacement rates to 3-D displacement rates based on geomorphological field observations. The ultimate goal is to illustrate how the survey with a portable radar interferometer paired with enhances campaign planning allows the quantification of continuous slope deformation at a highest possible resolution currently available for rugged Alpine terrains.

II. Physiographic and Geological Setting

The Illgraben debris flow catchment is a tributary basin located in the Rhone-Valley, Central Swiss Alps (Fig. 1) and has a relief of about 2100 meters, extending from the summit of the Illhorn at 2716.5 m a.s.l. to the confluence of the Rhone River located at about 610 m a.s.l. The northwestern flank of the catchment (Gorwetschgrat, Fig. 1) has a slope angle of about 50° and consists of a steeply dipping suite of thick-bedded dolomites and marbles [6]. The opposite southeastern valley flank [Fig. 2(a)] is separated by a fault zone trending SW-NE along the main channel. This flank dips at 40° and comprises an irregular alternation of highly fractured lithologies including quartzites, meta-conglomerates, dolomites, and low-grade gneisses [6]. The escarpment, where rock slope failures have recently released large volumes of sediment into the main channel encompasses the entire cirque between the Illhorn peak and the Gorwetschgrat further to the northwest. The catchment is exceptionally active with a mean annual erosion rate of 0.39 ± 0.03 m $\times$ yr^{-1}[4]. Many landslides (volumes up to a few thousand m^3) have been observed based on comparative analysis of aerial photographs [3]–[5] in an 4.6 km^2-wide sub-catchment. This area has supplied most sediment into the main channel in recent decades through landsliding. Accordingly mass failure in this area is of importance because they have generated dams in the trunk channel and resulted in in large hazardous debris flows [7]. Most of these landslides have originated from the upper regions of the cliff face [3] where the radar was directed for this study.

III. Method

A. Ground-Based Radar Interferometry

Ground-based radar interferometric measurements were made using the Gamma Portable radar Interferometer (GPRI). The GPRI is an real aperture radar, operating at a frequency range of 17.1–17.3 GHz. Two versions of the instrument were used in this study, GPRI-I and -II. GPRI-II [8] is a further development of GPRI-I [9], [10] and includes better focused antennas and allows full 360°-acquisition in 36 s instead of 37 min. Data was acquired over three measurement campaigns from two fixed positions (P1 and P2 in Fig. 1). Table I shows the details of the single measurement campaigns including date of acquisition, and time span when measurements were taken. Position P1 is situated on a 15 $\times$ 5 m wide, treeless platform at the edge of the escarpment, thereby providing a good view to the target rock slope. The GPRI was relocated to position P2 (Fig. 1) for the September 2010 acquisitions due unexpected road construction works preventing access to position P1. Position P2 was located 0.5–1 km from the target area upon a small 3 $\times$ 3 m wide platform, however the look direction was characterized by a smaller LOS sensitivity in the expected dominant displacement vector direction [$\hat{d}_{est}$, Fig. 2(b)], particularly in the lower part of the hillslope. For all campaigns the GPRI was set up on a geodetic tripod.

TABLE I
RADAR CAMPAIGN OVERVIEW

Nr.	Start Date/Time	End Date/Time	Nr. Scenes	Chirp length [ms]	Temporal baseline [min]	Azimuth width [degrees]	Weather condition	Position
1	23.09.2010 16:36 UTC	24.09.2010 13:32 UTC	159	2	10	60	cloud free	P2
2	10.06.2011 21:18 UTC	12.06.2011 11:06 UTC	227	2	10	50	1st day: cloud free 2nd day: clouded	P1
3	04.10.2011 11:43 UTC	05.10.2011 11:45 UTC	147	2	10	50	cloud free	P1

B. Interferometric Postprocessing

The measured total interferometric phase (φ_{int}) is made up of four linear contributions [11]

$$\varphi_{int} = \varphi_{topo} + \varphi_{disp} + \varphi_{atm} + \varphi_{noise} \tag{1}$$

Only the displacement phase (φ_{disp}) is needed for deformation measurements. Therefore, the remaining phases are subtracted from φ_{int}. The topographic phase contribution (φ_{topo}) is zero because of the perfect reposition of the GPRI. Phase noise (φ_{noise}) is defined by the signal-to-noise ratio (SNR) and ranges between 10 and 30 dB from 18.1° to 1.81°[8].

The remaining atmospheric phase contribution (φ_{atm}) is a function of pressure (P), temperature (T), and water vapor content (H) in the atmosphere and thus of the air refractive index N [12]. Because these parameters can vary rapidly in space and time, independent field determination of φ_{atm} is difficult for the same spatial extent that is covered with the radar acquisition, especially where the terrain has a large variation in elevation, exposure, relief and gradient.

The separation of φ_{atm} and φ_{disp} was done by modeling the atm from the data. The basic idea is to mask areas that show displacement after visual inspection, interpolate the phase over these areas and then compute the atmospheric contribution using a low-pass filter. Different filter sizes can be used to accommodate for different situations. The temporal distribution of the phase differences in the target area is shown in Fig. 3. Additionally, the spatio-temporal appearance of the measured and calculated phase differences can be seen for the $n-1$ interferograms in Appendix 1a and for the $n-(n-1)$ interferograms in Appendix 2a.[1] Strong spatial variability of up to 6 π is observed around 11:30 UTC. For each differential interferogram φ_{atm} was computed using a 2-D low-pass filter. Areas where displacement was observed were masked and the phase interpolated. The displacing areas were localized by looking at the stack of unfiltered interferograms and the identification of spatially coherent phase shifts. The outline of the mask applied on the interferograms is shown in Fig. 2(a). The temporal evolution of the unfiltered differential phase shows an increase in spatial variability between 05:00 UTC and 16:00 UTC. Therefore, different window sizes were used for the 2-D low-pass filters. During periods with low spatial variability an interpolation window size of 64 pixels was well suited to cover the rather large scale variations in the atmospheric phase contributions. While during the time-span mentioned above where strong small scale variations were dominating the scene signal, the sampling window size was reduced to 22 pixels.

The modeled φ_{atm} were removed from the scenes now only remaining φ_{disp}. The situation of the single interferograms after φ_{atm}-removal is shown in Appendix 1b for $n-1$ interferograms. Finally, the scenes were unwrapped and converted to LOS displacements. Daily LOS displacement rates were calculated by stacking and normalizing single displacement maps using a phase reference center, which was considered to be stable over the observation timespan [φ_{ref} in Fig. 3(a)].

C. Solar Radiation Model

Temporal evolution of the unfiltered $n-(n-1)$ interferograms show highly variable φ_{atm} during times with high solar radiation (Appendix 2a and c). Observations made in [13], showed that atmospheric disturbances under cloud-free conditions, are due to heat flux in the air mass driven by differences in the solar radiation var_{insol}. Thus, we introduce a simple proxy for the prediction of the spatial and temporal variability of φ_{atm}

$$var_{\varphi,atm}(t) \sim var_{insol}(t). \tag{2}$$

For a qualitative assessment of the atmospheric influence on the measurements, the solar radiation for the duration of the two surveys on the target area was modeled (see Appendix 2b). Here, we used a digital elevation model (DEM) with an resolution of 2 × 2 m as basis for the solar radiation model. The calculation was performed using the algorithm developed by [14] on a quarter hour basis. The dimensionless spatial variability of the insolation pattern at a given time is determined by calculating the 1-D spatial variance of the solar radiation affecting the identical spatial extent as the radar observation. The calculated variances of the two dates were normalized and plotted in Fig. 3(b) and (c) as well as for the August 2011 campaign in Appendix 2d. The contribution φ_{atm} on the measurements, determined by considering the φ_{disp} was found to be negligible within 10 min with regard to φ_{atm}. Accordingly, the measured phase contribution equals φ_{atm} [e.g., Fig. 3(a)]. A 1-D variability of every single scene was calculated in areas with a coherence coefficient $(|\gamma|) < 0.85$ and normalized to 1 (see Fig. 3 and Appendix 2c).

[1]The Appendices for this letter are available online in AVI format as supplementary material at http://ieeexplore.ieee.org.

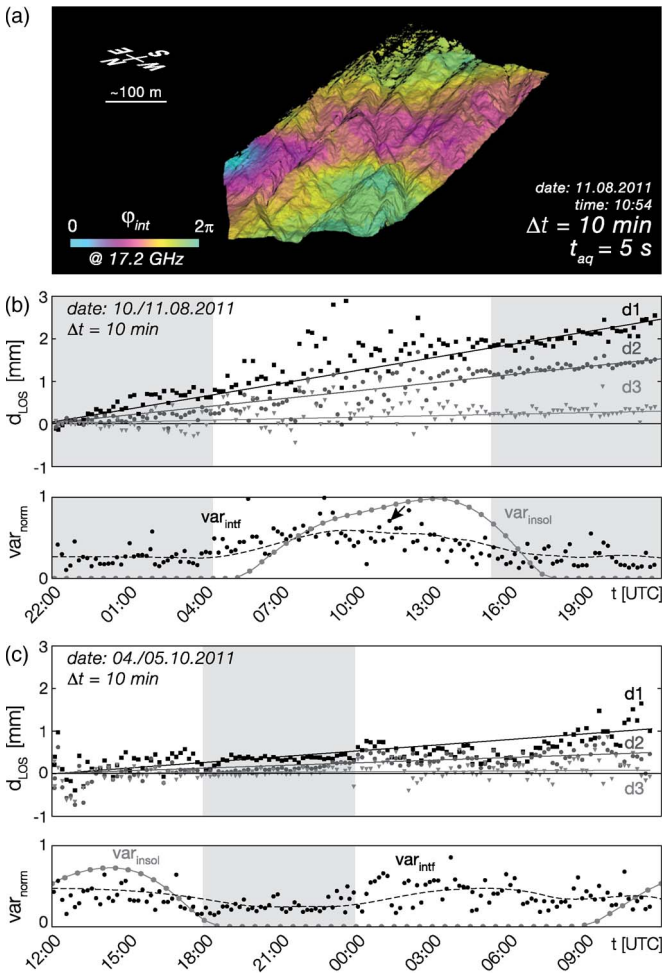

Fig. 3. (a) Differential interferogram with 10 min temporal baseline (Δ_t). The range of the phase differences (φ) covers a phase cycle. The single scene acquisition duration (t_{aq}) is 5 s. Same extent and view direction as in Fig. 2(b) and (c): 24 h cumulative LOS displacements (d_{LOS}) for points d1, d2, d3 [location see Fig. 2(e) and (f)]. Each data point represents the displacement in a time interval of 10 min. For each interferometric scene, a normalized spatial variability (var_{norm}) was calculated (var_{intf}). The interferometric variability is plotted against the modeled variability of the insolation (var_{insol}) hitting the target area. Dashed line: smoothed moving average of 5 data points. The shaded areas mark times with low atmospheric variability in the measured scenes.

D. Geometric Correction of LOS Displacement

The measured displacement represents only the landslide movement in direction of the line of sight (LOS), yielding estimates of displacement rates. A correction of the displacement to obtain the effective 3-D displacement lengths ($|\vec{d}_{tot}|$) was applied

$$|\vec{d}_{tot}| = \frac{|\vec{d}_{LOS}|}{cos(\vartheta)} \tag{3}$$

where ϑ is the angle between the LOS vector $\vec{d}_{LOS}$ to the corresponding ground pixel and the displacement vector $\vec{d}_{est}$. The sensitivity of the measurements along LOS relative to the slip direction decreases to zero where the LOS and the displacement direction are perpendicular to each other. Since the 3-D orientation of the displacement vector cannot be determined with only a single interferometric observation, the apparent displacement direction was corrected with the orientation of the slip plane that was measured in the field (dip azimuth and angle, where accessible) and from the TLS surface-model. We also used the orientation of strained roots, spanning across a fault scarp in the accessible upper part of the instability [Fig. 2(a)], to determine the direction of slip. The estimated displacement vector [unit vector: $\hat{d}_{est}$ in Fig. 2(b)], as well as the LOS fractions per resolution cell were calculated using (3) for the two observation points P1 and P2 [Fig. 2(b)]. The bottom line for these calculations were assumptions that that deformation was homogeneously distributed over the entire rockslide. Supporting evidence is provided by the absence of longitudinal and vertical cracks.

IV. Results

A. Atmospheric Phase Variability

The measurements show that the calculated phase variability increases during daytime and decreases after sunset (Appendix 2) similar to the modeled temporal evolution of the insolation variability during cloudless days (Appendix 2c). We observed that the atmospheric turbulence started about 1 h before the sun directly illuminated the scene. Note that the campaign in October 2011 yielded in general a lower variability in the data [Fig. 3(c)] as in August 2011. However, the variability in October 2011 increased after midnight. We relate this observation to the effect of substantial dew in the target area. The phase variabilities of the extended observation period in the August 2011 (Appendix 1a and c) during daytime of 12.08.2011 indicates comparable low variabilities as during the night-time. It was observed, that the weather situation during this time-span was cloudy, therefore no direct insolation was hitting the observation area. After filtering, the temporal point displacement (Fig. 3(b) and (c) and Appendix 1c and d) reveals a standard-deviation σ of the single observations, which ranges from 0.20–0.25 mm during stable atmospheric conditions to σ of 0.45–0.50 mm during phases with high insolation differences. Although the atmospheric filtering led to a reduction of σ from 0.90 to 1.00 mm prior to the filtering, this is still highly variable.

B. Slope Deformation Analysis

The geometrically and atmospherically corrected 24 h displacement rates of the different surveys are shown in Fig. 3(d)–(f); the total displacement after 55 days is illustrated in Fig. 2(c). Daily total displacement rates of up to 3 mm were measured in September 2010 as well as in August 2011 at the top western part of the analyzed escarpment. The spatial distribution of the deformation signal implies a distinct boundary between the displaced mass and the stable surrounding areas. This result is in good agreement with field-observations in the top and western part of the rockslide, where the spatial extent is defined by the presence of fault scarps and the mapped slip plane. Displacement rates decreased to less than 1.5 mm between August and October 2011. The spatial pattern of the signal, however, remained constant. In September 2010 when scans were collected from site P1, the lower boundary of the rockslide was allocated to a higher elevation. Here, the LOS

fraction of the total displacement beneath 2100 m a.s.l. is less than 0.5. The corrected total displacement limit of 0.5 mm/day is above this height. The 24 h evolution of the displacement at selected points is illustrated in Fig. 3(b) and (c). Cumulative displacements are linear over time. Note that the values are LOS displacements. The averaged observations from August 2011 and October 2011 form one interferometric pair with a temporal baseline of 55 days. The resulting displacement [Fig. 2(c)] indicates that the upper part of the rockslide is strongly decorrelated because of the strong deformation. Hence, it is not possible to calculate displacement rates in these areas. In the lower part of the rockslide, deformation was still measurable due to the lower LOS dependence on deformation. The results of the measurements showed that the lower boundary of the moving zone was located at a lower elevation than was expected from the short time measurement due to the smaller LOS sensitivity in the lower part of the hillslope. The combination of the results of the short- and long-term observation, and particularly of the 55-day baseline data, resulted in the delineation of the lateral boundaries of the rockslide at a resolution of 5 m, yielding a cross-sectional width of approximately 130 m and a length approaching 360 m. The orientation of the slide plane is determined through field measurements and results in a perpendicular thickness of the slope instability of about 5–15 m. These constraints yield an estimated volume of a potential slope-failure of approximately 0.5×10^6 m^3.

V. Summary and Conclusion

Terrestrial radar interferometry is a powerful method to obtain deformation data with high temporal and spatial resolution, particularly for the rapid identification and interpretation of land- and rockslides. The atmospheric influence on radar propagation time strongly depends on changes in the air refractive index N. The resulting perturbation can be mapped as a consequence of the relatively short acquisition time of the radar interferometer, allowing almost complete removal of the atmospheric contribution from the measured phase shift during times with low phase variabilities. This substantially increases the precision of the retrieved deformation information both in space and time, as illustrated here. Likewise, it is also shown that the highly variable atmospheric phase is strongly correlated to high insolation differences. This results in the situation where the removal of the atmospheric phase contribution during highly variable atmospheric conditions is not sufficient with respect to the achievable precision of the method. Therefore, we propose that the here presented proxy for the prediction of atmospheric phase variability can be used for the planning of short term measurement campaigns, avoiding periods with highly variable atmospheric phase contributions.

Finally, the presented approach here, which includes: atmospheric phase filtering, geometric correction of the measured displacement data, data about LOS displacement lengths and geologic field observations permits the determination of the 3-D displacement magnitude. This correction facilitates comparison between displacement data collected with either radar interferometry from different survey sites, or other high-resolution techniques (e.g., GPS-based displacement fields). The survey strategy presented herein allows rapid determination of the spatial and temporal behavior of slope instabilities with relatively low effort, which is of importance to support hazard investigations where decisions about natural hazards and public safety may have to be made within a short time, and at low costs.

Acknowledgment

Part of this work was supported through the Swiss initiative to foster and promote Swiss scientific and technological competences related to space activities by the Swiss Space Office of the Swiss State Secretariat for Education and Research.

References

[1] F. Imaizumi, R. C. Sidle, S. Tsuchiya, and O. Ohsaka, "Hydrogeomorphic processes in a steep debris flow initiation zone," *Geophys. Res. Lett.*, vol. 33, no. 10, p. L10404, May 2006.

[2] R. M. Iverson, M. E. Reid, and R. G. LaHusen, "Debris-flow mobilization from landslides1," *Annu. Rev. Earth Planet. Sci.*, vol. 25, no. 1, pp. 85–138, May 1997.

[3] C. Berger, B. W. McArdell, and F. Schlunegger, "Sediment transfer patterns at the illgraben catchment, switzerland: Implications for the time scales of debris flow activities," *Geomorphology*, vol. 125, no. 3, pp. 421–432, Feb. 2011.

[4] G. Bennett, P. Molnar, H. Eisenbeiss, and B. McArdell, "Erosional power in the swiss alps: Characterization of slope failure in the illgraben," *Earth Surface Process. Landforms*, vol. 37, no. 15, pp. 1627–1640, Dec. 2012.

[5] F. Schlunegger, A. Badoux, B. W. McArdell, C. Gwerder, D. Schnydrig, D. Rieke-Zapp, and P. Molnar, "Limits of sediment transfer in an alpine debris-flow catchment, illgraben, switzerland," *Quaternary Science Reviews*, vol. 28, no. 1/112, pp. 1097–1105, Jun. 2009. Natural Hazards, Extreme Events and Mountain Topography.

[6] J. Gabus, M. Weidmann, P. Bugnon, M. Burri, M. Sartori, and M. Marthaler, "Geological map of sierre 1 : 25 000 (lk1287, sheet 111)," *Geological Atlas of Switzerland*, Swiss Geological Survey, Bern, 2008.

[7] A. Badoux, C. Graf, J. Rhyner, R. Kuntner, and B. McArdell, "A debris-flow alarm system for the alpine illgraben catchment: Design and performance," *Nat. Hazards*, vol. 49, no. 3, pp. 517–539, Jun. 2009.

[8] C. Werner, A. Wiesmann, T. Strozzi, A. Kos, R. Caduff, and U. Wegmüller, "The GPRI multi-mode differential interferometric radar for ground-based observations," in *Proc. 9th EUSAR*, 2012, pp. 304–307.

[9] C. Werner, A. Wiesmann, T. Strozzi, and U. Wegmüller, "Gamma's portable radar interferometer," in *Proc. 13th FIG Int. Symp. Deformation Meas. Anal./4th IAG Symp. Geodesy Geotech. Struct. Eng.*, 2008, pp. 1–10.

[10] A. Wiesmann, C. Werner, T. Strozzi, and U. Wegmüller, "Measuring deformation and topogrphy with a portable radar interferometer," in *Proc. 13th FIG Int. Symp. Deformation Meas. Anal./4th IAG Symp. Geodesy Geotech. Struct. Eng.*, 2008, pp. 1–9.

[11] R. Bamler and P. Hartl, "Synthetic aperture radar interferometry," *Inverse Problems*, vol. 14, no. 4, p. R1, Aug. 1998.

[12] A. Ishimaru, *Wave Propagation and Scattering in Random Media/Akira Ishimaru*. New York, NY, USA: Academic, 1978.

[13] A. P. Weigel and M. W. Rotach, "Flow structure and turbulence characteristics of the daytime atmosphere in a steep and narrow alpine valley," *Q. J. R. Meteorol. Soc.*, vol. 130, no. 602, pp. 2605–2627, Oct. 2004..

[14] P. Rich, R. Dubayah, W. Hetrick, and S. Saving, "Using viewshed models to calculate intercepted solar radiation: Applications in ecology," *Amer. Soc. Photogramm. Remote Sens. Tech. Papers*, pp. 524–529, 1994.